GAMMA RAY EMISSION FROM THE DRAGONFLY PULSAR J2021+3651

Margherita De Toma

8 may 2021

Abstract

This paper analyzes the detection of pulsed gamma-rays from the Dragonfly Pulsar (PSR J2021+3651) using data acquired with the Large Area Telescope (LAT) on board the Fermi Gamma-ray Space Telescope. In particular, the analysis focuses on searching for changes in the rotational frequency of the pulsar due to a slow release of rotational energy.

Contents

1 Introduction

1.1 Pulsar first order approximation model

Pulsars are rotating neutron stars characterized by high magnetic fields and electromagnetic emissions related to frequency slowing down over time. One useful parameter in the pulsar model is the pulsar period P.
At first order and at some distance from the star, it's possible to assume a magnetic dipole emission, from which:

$$P_{rad} = \frac{2}{3}\frac{(\ddot{m}_\perp)^2}{c^3}. \tag{1}$$

where $\ddot{m}_\perp$ is the ortogonal component of the pulsar magnetic dipole moment which is not usually aligned to the rotation axis but spins around it causing the pulsed appearance of emission.
The rotational energy is related to the period and moment of inertia I by:

$$E_{rot} = \frac{1}{2}I\Omega^2 = \frac{2\pi^2 I}{P^2}. \tag{2}$$

Knowing the period and his time derivative $\dot{P}$, it's possible to compute the energy lost in time:

$$\frac{dE_{rot}}{dt} = -\frac{4\pi^2 I\dot{P}}{P^3} \tag{3}$$

also known as *spin-down luminosity*.

1.2 Detector introduction

The LAT is a gamma-ray detector on board the Fermi Gamma-ray Space Telescope. It's a pair-production telescope which detects photons with energy from 20 MeV to 300 GeV with a field of view of 2.4 sr. Each event recorded with the LAT is associated to a time value that derives from the GPS clock aboard Fermi, which defines MET (Mission Elapsed Time) that corresponds to the number of seconds since January 1, 2001, at 0h:0m:0s in the Coordinated Universal Time (UTC) system. Ground tests demonstrate that the LAT measures time with accuracy $\leqslant 1\mu s$ [4].
All the following time events will be expressed in MET.

2 Data selection

The data has been downloaded from Fermi Science Support Center web page in the section dedicated to LAT Data [2].
The web site provides *fits* file of events (FT1 files) and FT2 files, containing the Spacecraft data.

In the following, it's reported the ephemeris of PSR J2021+3651 used for the following analysis [1].

Pulsar name	J2021+3651
Right Ascension (J2000)	20:21:05.46
Declination (J2000)	36:51:04.8

It has been performed a data selection using the *Fermi* Science Tools developed by the FSSC and instrument teams[2] that are accurate until a few μs for isolated pulsars [1]. The Fermi position uncertainty is here negligible.
The data analysis below has been implemented using Pandas library and Astropy package from Python.
Using *ftselect* and *gtmktime* tools, we have selected events within a radius of 3 degrees, with energy $>$ 100 MeV. To avoid collecting photons coming from Earth processes, the field of view has been restricted up to 90 degree from the zenith that is the angle between the reconstructed event direction and the zenith line (that originates at the center of the Earth and passes through the center of mass of the spacecraft)[3].
Afterwards, the data have to be centered in the Solar System barycenter. This is necessary to successfully measure the deviation in pulsar rotational frequency. In fact, there are some not negligible time intervals to be added to correct the LAT measure. This is due to:

- the spacecraft revolution around the Earth and the Sun;
- the "Shapiro delay" caused by the Sun gravitational field;
- geometrical light delay ("Roemer" effect);
- special relativity correction to the speed of the Earth;
- revolution delay if the pulsar belongs to a binary system.

The tool *gtbary* takes all of these effects into account and computes corrections.

3 Analysis

3.1 Timing model

As the loss of rotational energy is sufficiently slow, it's possible to Taylor expand in time the pulsar frequency:

$$f(t) = f(t_0) + \dot{f}(t_0)(t-t_0) + \frac{1}{2}\ddot{f}(t_0)(t-t_0)^2 + \mathcal{O}(t^3)$$

where t_0 is the central value of the series expansion, called *epoch*. Here, we have $t_0 = 247545009.147469(1)$.
The number of rotations is related to the frequency as:

$$dN = f(t)dt = [f(t_0) + \dot{f}(t_0)(t-t_0) + ...]dt \quad (4)$$

and, integrating in time and taking the result fractional part, we obtain the phase shift:

$$\phi(t) = \phi(t_0) + f_0(t-t_0) + f_1(t-t_0)^2 + .. \quad (5)$$

where $f_0 = f(t_0)$ and $f_1 = \dot{f}(t_0)$.
In the following analysis, we have stopped at the first-order derivative.

3.2 Timing solutions

For each photon, we have reduced the arrival time to a phase value in the interval 0 to 1 using the relation:

$$\phi_i \equiv \phi(t_i) \simeq \phi(t_0) + f_{0,\alpha\beta}(t_i - t_0) + f_{1,\alpha\beta}(t_i - t_0)^2$$

where i runs over the number of photons (N) while α and β define a grid search of test values for f_0 and f_1.

3.2.1 Periodicity test: Z_n^2

The test Periodicity test is an hypotheses test which propose to detect small deviations from periodicity starting from approximate values.
In this case, it has been implemented the Z_n^2 test [3] to compute the best f_0 and f_1 that describes the pulsar by means of the statistical variable Z_n^2:

$$Z_n^2 = \frac{2}{N}\sum_{k=1}^{n}\left[\left(\sum_{i=1}^{N} cos(2\pi k\phi_i)\right)^2 + \left(\sum_{i=1}^{N} sin(2\pi k\phi_i)\right)^2\right]$$

[1] RA, Dec coordinates from https://fermi.gsfc.nasa.gov/ssc/data/access/lat/ephems/lat_psrcat/radio/ephem_J2021+3651_gbt.par
[2] http://heasarc.gsfc.nasa.gov/lheasoft/ftools
[3] https://fermi.gsfc.nasa.gov/ssc/data/analysis/documentation/Cicerone/Cicerone_Data/LAT_Data_Columns.html

where n is the number of harmonics, set equal to 5.
The best value for f_0 and f_1 corresponds to the ones that maximizes the Z_n^2.

Computation It has been implemented a program in Python which tries all the combination of (f_0, f_1) from a given set of "try-values" to find the couple that maximize the Z_n^2.
For the first run, the "try-values" has been generated using a matrix of values defined by:

$$[f_0 - 500df_0, f_0 + 500df_0] \times [f_1 - 25df_1, f_1 + 25df_1]$$

with steps $df_0 = 0.1/T$ and $df_1 = 1/T^2$ respectively, where $f_0 = 9.63935\ s^{-1}$ and $f_1 = -8.8892 \times 10^{-12}\ s/s$.
This test has been implemented 6 times, each one operating with the f_0 and f_1 estimations of the previous run as "start-values" and with steps one order of magnitude lower. In Fig. 2 the first four steps of the test are shown. We can clearly see the computational convergence looking at the progressive approach to the yellow zone corresponding to the set of higher Z_n^2 values. Note that already at the fourth step, we are loosing the computational sensibility to go much further.
The estimates for each run have been reported in Table 1.
The error for f_0 and f_1 has been taken equal to their corresponding *step* used to compute the test.
In Fig. 1, it's shown a plot of the phase as a function of time using the approximated expression in equation (5) and the f_0 and f_1 values computed in the runs. We can immediately note that, going through runs, the phase plot is increasingly constant with time, indicating that the f_0 and f_1 estimations converge to the values that better represent data.

f_0 [Hz]	f_1 ($\times 10^{-12}$) [s/s]
9.63934484(1)	-8.89(2)
9.639344848(1)	-8.888(2)
9.6393448475(1)	-8.8870(2)
9.63934484746(1)	-8.88699(2)
9.639344847458(1)	-8.886980(2)
9.6393448474592(1)	-8.8869796(2)

Table 1: f_0 and f_1 running estimations

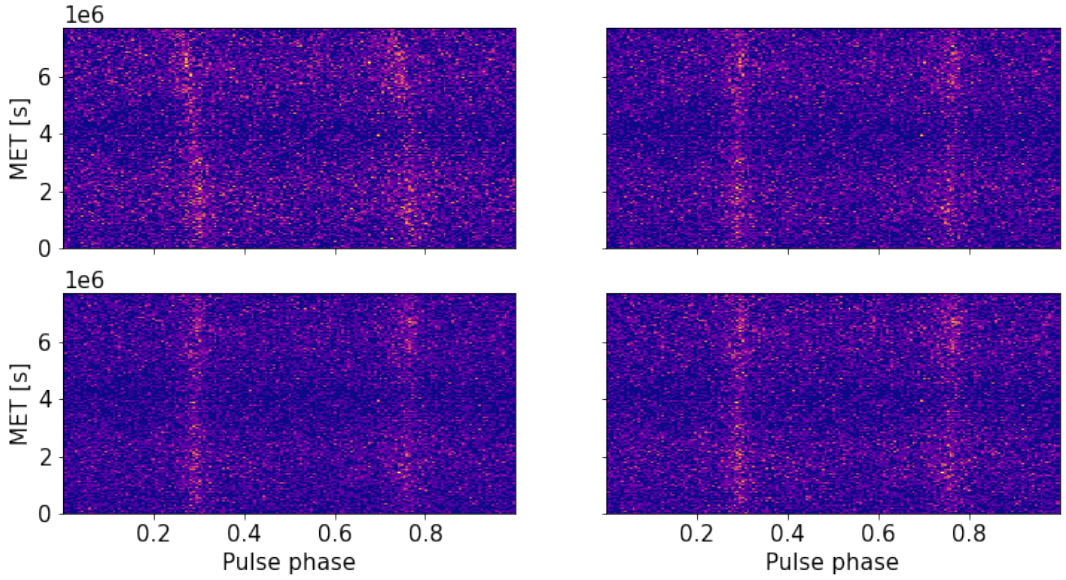

Figure 1: Phase evolution in time. The phase has been artificially shifted by 0.2 to better visualize also the second peak. Furthermore, we have omitted to show the phase plot of the last two runs because the difference from the third and fourth was not evident from figures.

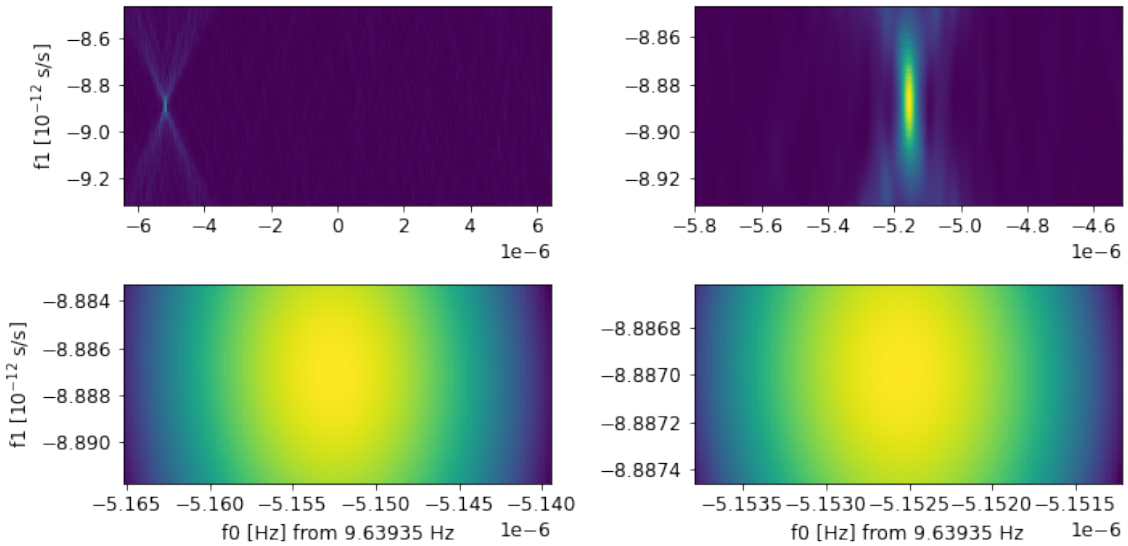

Figure 2: Run steps for f_0 and f_1 computation.

3.3 Phasogram and energy map

For the following analysis, we have used the parameters estimated in the last run, that are (Tab. 1):

$$f_0 = 9.6393448474592(1) \quad \text{Hz} \tag{6}$$

$$f_1 = -8.8869796(2) \times 10^{-12} \quad \text{s/s} \tag{7}$$

from which:

$$P = 1/f_0 = 0.10374149030093(1) \quad \text{Hz} \tag{8}$$

$$\dot{P} = -f_1/f_0^2 = 0.095644312198351(3) \quad \text{s/s} \tag{9}$$

In Fig. 3 are shown phase histograms ("*phasograms*") binned at 0.01 in 3 different energy ranges: over 100 MeV, 100 MeV - 1 GeV and over 1GeV. In each one, there are two peaks: the first peak (P1) is found to be about in the phase interval $0.24 < \phi < 0.35$ and the second (P2) between about $0.69 < \phi < 0.82$.
For all phasograms, have been estimated the phase difference between P1 and P2 and the ratio between counts at peaks (Table 2). Regarding the error over phases, it has been set equal to one bin since the error over time from the error propagation in eq. (5) is neglectable.

It has been assumed that the counts over a bin follow a poissonian statistics. In fact, we can assume all the requirements for the poissonian distribution:

- two events cannot occur at exactly the same instant;
- for time intervals much shorter than the pulsar's period (in 8), we can assume that events occur independently;
- the average rate at which events occur is independent of any occurrences.

Consequently, the counts error over bin has been set equal to $\sqrt{N}$, being N the counts.
Both peaks fade with increasing energy, but P2 is always lower than P1, except than in the highest energy range.
Then, have been realized a 2D histograms showing events in different energy ranges with thickness equal to 300 MeV, to leave no counts resulting from larger interval choices (Fig. 4). It's evident that most of the photons have energy between $100 - 400$ MeV.

Energy range	$\Delta\phi$	counts(P2) / counts(P1)
$>$ 100 MeV	0.4700 ± 0.014	0.94 ± 0.08
100 MeV - 1 GeV	0.4700 ± 0.014	0.88 ± 0.09
$>$ 1GeV	0.4700 ± 0.014	1.2 ± 0.2

Table 2: Phasogram phase shift and ratio between values at peaks.

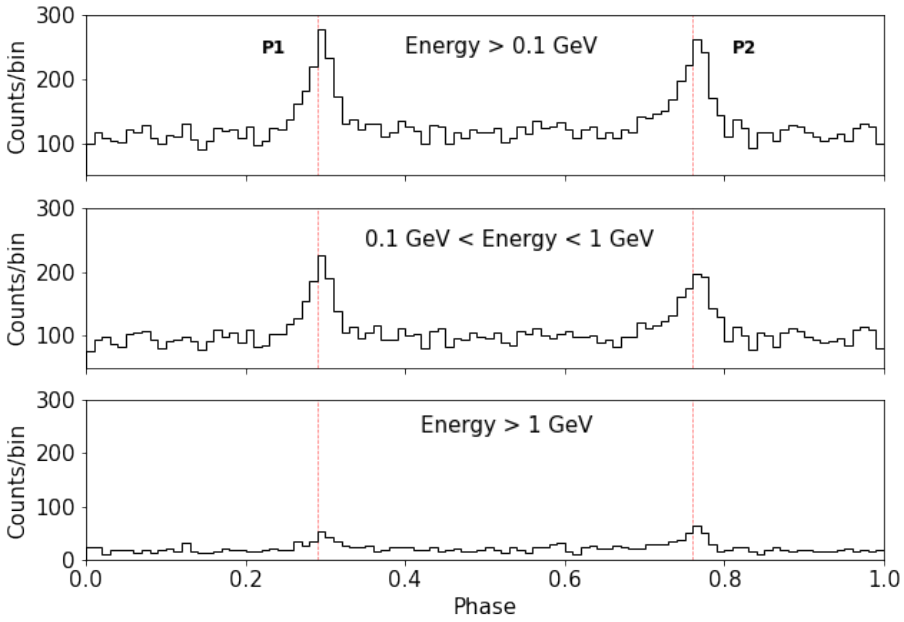

Figure 3: Phasogram in 3 different energy ranges. The phase has been artificially shifted by 0.2 to better visualize also the second peak.

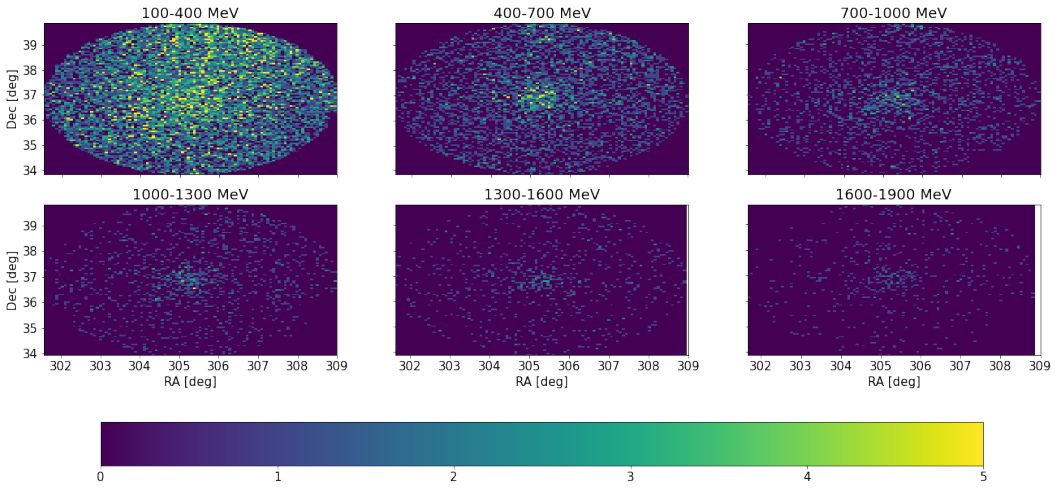

Figure 4: 2D histograms in energy ranges of 300 MeV each. All the histograms have the same *colorbar* scale.

3.4 Pulsar characterization

Approximating the pulsar as a rotating magnetic dipole, we can compute some characteristic quantities.
The magnetic field produced by a magnetic dipole is:

$$B = \left(\frac{3c^3 I}{8\pi^2 R^6}\right)^{1/2} \left(P\dot{P}\right)^{1/2}$$

which can be estimated using a typical moment of inertia [4] of 10^{45} g·cm^2 for a neutron star and

[4] Assuming spherical geometry: $\mathrm{I} = \frac{2}{5}\mathrm{MR}^2$

$R \simeq 12$ km [5]. We obtain:

$$B \simeq 5.9 \times 10^{18} \left(P\dot{P}\right)^{1/2} \text{Gauss}$$

The *characteristic age* is instead defined as:

$$\tau \equiv \frac{P}{2\dot{P}}$$

Using the previous estimates for P and $\dot{P}$, we can then evaluate B, τ and the *spin-down luminosity* (eq. (3)). The results are presented in Tab. 3.

Finally, we have realized a diagram of P and $\dot{P}$(Fig. 5), showing the pulsar population [6]. Have been also reported the lines for which B, τ and $\dot{E}$ are constant. The red dot corresponds to PSR J2021+3651 with P and $\dot{P}$ from Tab. 3.

4 Conclusions

As result of this analysis, the Dragonfly Pulsar appears to belong to the family of the youngest pulsar that populates the upper right region of the diagram. In fact, it has a relatively high magnetic field $B \simeq 10^{13}$ Gauss, *characteristic age* $\simeq 10^4$ yr, P$\simeq 0.1$ s and $\dot{P} \simeq 10^{-12}$ s/s.

P	0.103741490300929(1) s
$\dot{P}$	9.5644312198351(3) $\times 10^{-14}$ s/s
$\dot{E}_{rot}$	-3.3819053(6)$\times 10^{36}$ erg/s
τ	17197.160(3) y
B	3187541104038.445312500(3) Gauss

Table 3: Pulsar characteristic quantities.

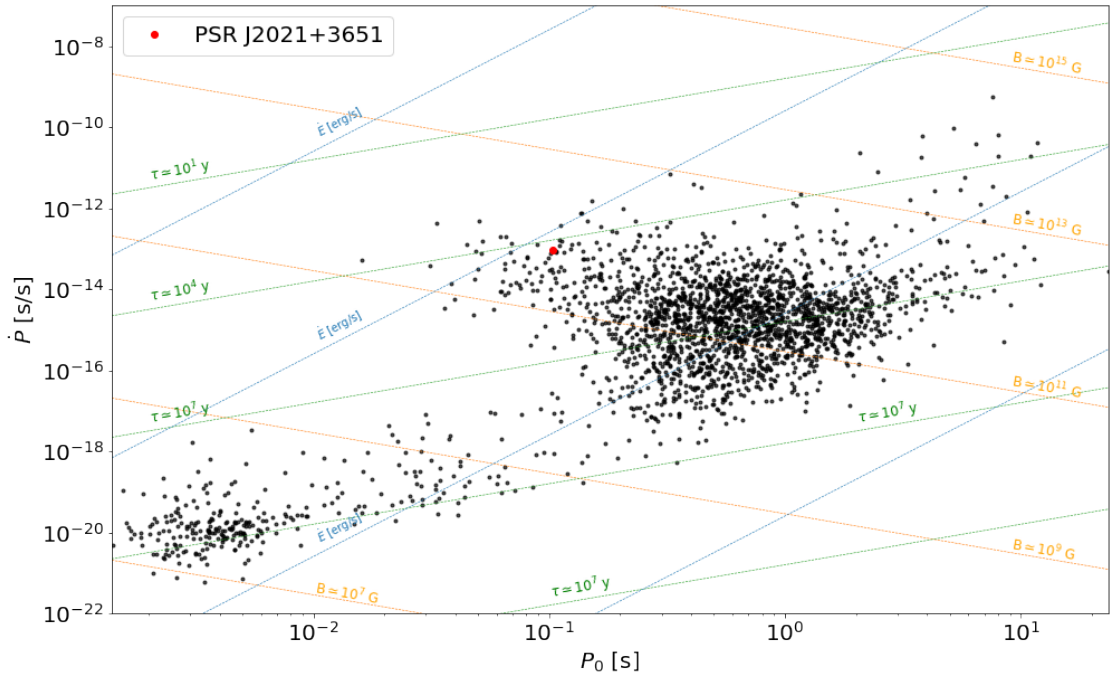

Figure 5: Plot of period VS its first time derivative. Data from ATNF Pulsar Catalogue [7].

References

[1] Smith, D. A., Guillemot, L., & Camilo, F. et al. 2008, A&A, 492, 923

[2] Fermi NASA data access.

[3] R. Buccheri et al., Search for pulsed γ-ray emission from radio pulsars in the COS-B data, Astron. & Astrophys. 128, 245-251, (1983)

[4] A.A. Abdo et al., Pulsed Gamma-Rays from PSR J2021+3651 with the FERMI Large Area Telescope, The Astrophysical Journal, 700:1059–1066, 2009 August 1

[5] J. Nättilä et al., Neutron star mass and radius measurements from atmospheric model fits to X-ray burst cooling tail spectra, Astronomy & Astrophysiscs, A&A 608, A31 (2017)

[6] R. N. Manchester et al., The Australia telescope national facility pulsar catalog, AJ, 129, 1993-2006 (2005).

[7] ATNF Pulsar Catalogue.